Computational Materials Science 247 (2025) 113538

Contents lists available at ScienceDirect

Computational Materials Science

journal homepage: www.elsevier.com/locate/commatsci

Full length article

Size scalability of Monte Carlo simulations applied to oxidized polypyrrole systems

Greg Helmick, Yoseph Abere, Estela Blaisten-Barojas *

Center for Simulation and Modeling (former Computational Materials Science Center), George Mason University, Fairfax, VA 22030, USA
Department of Computational and Data Sciences, George Mason University, Fairfax, VA 22030, USA

ARTICLE INFO

Keywords:
Polypyrrole
PPy
Metropolis Monte Carlo simulation
Coarse grained force field
Glass transition temperature
CPU–GPU

ABSTRACT

Oxidized polypyrrole (PPy) is a conducting polymer with diverse applications such as supercapacitors, sensors, batteries, actuators, neural prosthetics, among others. PPy is most commonly synthesized for the specific application yielding low molecular weight oligomers that form amorphous polymer matrices. Hence, molecular simulation analyses are challenging. This work generalizes the recently proposed coarse grained force field (CGFF) for halogen oxidized PPy in the condensed phases and introduces a novel implementation of the Monte Carlo (MC) simulation based on the CGFF that enables simulations of polymer systems with more than 100000 particles. The MC implementation utilizes a combination of CPU and GPUs and exploits a numerical approximation based on polynomial piecewise interpolation for the calculation of the CGFF pairwise additive terms. The MC simulations evidence that the oxidized PPy thermodynamic and structural properties are consistent as the system size is scaled up. Predicted properties include density, enthalpy, potential energy, heat capacity, coefficient of thermal expansion, caloric curve, glass transition temperature range, compressibility, bulk modulus, radial distribution functions, and polymer chain characteristics. The oxidized PPy samples display oligomer chain stacking that persists with temperatures up to the glass transition. Simulated properties are consistent with experimental observations when available and predict trends in all other cases.

1. Introduction

The discovery of conjugated organic polymers with conducting and semiconducting properties in the 1970's allowed the development of novel applications for the new family of polymers, commonly termed organic metals [1]. Oxidized polypyrrole (PPy) is one of these organic metals with multiple applications including super capacitors, sensors, batteries, coatings, actuators, neural prosthetics, and drug delivery among others [2–5]. Polypyrroles synthesize readily either chemically or electrically as well as being low cost [6,7]. These attributes make PPy an empirically well portrayed polymer [8,9]. A specific characteristic of oxidized PPy is that synthesis protocols produce short oligomers of low molecular weight between 522–1173 u [10,11]. Hence, oxidized PPy polymer matrices are formed by packing these short oligomers and the oxidizing dopants. The donor–acceptor oxidation mechanism occurs between the oligomers and the dopants yielding n- or p-type semiconductors depending upon the oligomers donating electrons or acquiring them. Chemically, within oxidized PPy the oligomers acquire the quinoid phase in which there is a double carbon–carbon bond between the repeating pyrrole units (monomers) along the conjugated backbone, while the benzenoid phase establishes at reduction [12–14]. Based on such peculiarity, the oligomer chains are rigid and planar resembling flat sticks favoring chain stacking into columnar or lamella formations within the polymer matrix [15]. The conduction property of the oxidized PPy systems is based on polarons or bi-polarons, quasi-particles existing due to an alternation of regions with more or less localized charge along the oligomers backbone [16]. When dopants are eliminated from the oxidized PPy matrix, the oligomers neutralize, their chemical phase reverts to be benzenoid, the oligomers acquire flexibility, and the polymer matrix becomes an insulator. Macroscopically, upon reduction, the polymer matrix increases its volume up to 30%–35% [12,17].

With the empirical discovery of these structurally complex materials composed of many oligomer chains and the oxidizing dopants used in each synthesis scenario, efficient simulation methods become necessary for predicting their thermodynamic, mechanical and electronic properties at the nanoscale. Although density functional theory (DFT) may provide an excellent quantum approach for systems containing hundreds to a very few thousands of atoms, it is still limited to systems typically containing less than 1000 atoms [18]. To circumvent these limitations, the classical approach involves either, all-atom (AA)

---

[*] Corresponding author at: George Mason University, MSN 6A12, 4400 University Drive, Fairfax, VA 22030, USA.
E-mail address: blaisten@gmu.edu (E. Blaisten-Barojas).

https://doi.org/10.1016/j.commatsci.2024.113538
Received 8 September 2024; Received in revised form 10 November 2024; Accepted 11 November 2024

or coarse-grained (CG) classical force fields (FF) based on analytical models of the multiple interactions occurring in a system. CG models proclaim the ability of scaling up to larger systems of particles [19] together with enabling simulations of more complex molecular processes than AA models [20]. Currently, molecular dynamics (MD) and Monte Carlo (MC) are capable of incorporating AAFF or CGFF for simulation studies of the mechanical, thermodynamical, and selected structural properties of particle systems. Nonetheless, the existing AA force fields are parametrized on empirical properties of families of molecules, while the CGFF require a parametrization tailored to how the CG particles are constructed for each specific undertaken study.

Algorithmic improvements are crucial in all areas of high performance computing (HPC) whether targeting CPU, GPUs (graphics processing units) or a combination of the two [21,22]. Nowadays GPUs have become a staple of HPC environments and are incorporated in existing MC [23,24] and MD [25–27] implementations due to their high degree of parallelism [28] and yet addressing the stringent power cap and wire delay imposed by the hardware [28,29]. These advances in hardware and algorithms enable the simulation of systems of increasing complexity, size, and longer timescales [30,31].

In this work, we systematically investigate two directions that generalize our previous CGFF for reduced polypyrroles [32,33], further parametrized for PPy with chlorine (Cl) as the oxidizing agent [34], with system properties obtained by employing our custom Monte Carlo package that enabled the simulations of a small size PPy system containing 64 oligomers and 256 atomic dopants [34]. The first direction is broadening the application domain of the CGFF to be parametrized for three additional halogen dopants, fluorine (F), bromine (Br), and iodine (I). Additionally, our previous analytical description of the CGFF for PPy with oxidizing Cl dopants [34] is slightly modified to contain one parameter less. The second direction is the performance enhancement of the custom MC simulation implementation, enabling a substantial scaling up of the simulated system size to contain more than 100 000 particles.

The organization of this work is as follows. Section 1 gives an introduction about polypyrroles and polymer simulations employing Monte Carlo approaches. Section 2, Model and Methods, is partitioned into two subsections. Section 2.1 provides a description of the oxidized PPy system and the CGFF components with the mathematical expressions listed in Appendix A, together with the adopted formulae reducing the number of parameters. Section 2.2 entails an overview of the Metropolis Monte Carlo method, including a description of the custom workflow implemented in the simulations. Section 3, Results, is subdivided in three parts. Section 3.1 provides outcomes concerning the parametrization of the CGFF for the various dopant types, F, Cl, Br, and I. Section 3.2 expands on the novel implementation of the MMC in the isobaric–isothermal ensemble (NPT) on hybrid CPU–GPU computer platforms that enables scaling up the size of the system. Meanwhile, Section 3.3 describes results obtained applying the advances in the two previous subsections for calculating numerous oxidized PPy thermodynamic and structural properties. Section 4 outlines a few perspectives and Section 5 concludes this article. The Appendix B contains the Supplementary Information (SI), which brings forth multiple pertinent details.

2. Models and methods

2.1. The Coarse-Grained Force Field (CGFF)

Oxidized PPy samples contain both, PPy oligomers and oxidizing dopants, with a given relative concentration. Within the CGFF, each oligomer is represented by a short necklace-like chain of soft coarse grained (CG) spherical particles, where each CG particle represents the pyrrole monomer (Py) (C_4H_2NH) [34]. The CG particle mass is the Py monomer mass of 65.07 u, which occupies a volume large enough for accommodating the 5-member molecular ring. Additionally, each CG particle has a point charge q and a dipole moment $\vec{\mu}$ anchored at the sphere center; the latter points in the direction of the N atom. The oligomer end monomers have one extra H atom. These CG particles require six degrees of freedom to be moved, three translations and three rotations in a 3-D Euclidian space. The halogen dopants, F, Cl, Br or I, are represented as harder spheres with a point charge Q at their center requiring three translational degrees of freedom to be moved around. Throughout this work the CG particles are termed *monomers* and *dopants*. The oxidized PPy systems considered contain oligomers formed by twelve monomers with molecular weight of 782.9 u, termed 12-Py. Fig. 1 illustrates the all atom 12-Py oligomer and its CG representation. To simulate the condensed system, an almost cubic computational box is modeled containing N_{py} oligomers and N_{dop} dopants. A small system with 64 oligomers and 256 dopants is built by stacking Lego-like orthorhombic prisms with face-centered sites occupied by the centers of mass of four oligomers, each of them decorated with four dopants. The initial density of such system is around 1000 kg/m^3, it is first minimized and next NPT equilibrated at 600 K, 1 atm by a series of MMC long simulations. Systems of increasing size are supercells obtained by stacking replicas of the 600 K equilibrated system organized as described in Table SI.1 of the SI. Periodic boundary conditions in the three dimensions of these systems are employed throughout. Our study entails four different oxidized PPy samples, each of them containing the 12-Py oligomers and either one of the F, Cl, Br or I halogen dopants, with a relative concentration monomer:dopant of 3:1.

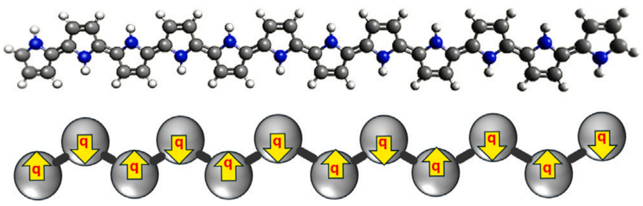

Fig. 1. Visual rendering of the 12-Py heterocyclic oligomer in the quinoid phase (top) with a schematic representation of its coarse grained view (bottom). The charge on each CG monomer is termed q and the dipole moment $\vec{\mu}$ is depicted with a yellow arrow.

The CGFF is composed of two analytical terms modeling the potential energy of the full oxidized PPy system: $U_{total} = U_{intra} + U_{inter}$ [34]. The U_{intra} term includes interactions within the oligomer chain, exclusively. Meanwhile, the U_{inter} term encompasses interactions between dopants, between monomers in one oligomer with all other monomers of different oligomers, and between monomers with dopants. Appendix A provides the analytical expressions of U_{intra} and U_{inter} in Appendices A.1 and A.2, respectively. This CGFF has 22 parameters. Twelve of those parameters are unique to U_{intra}, their values were evaluated previously [34] and are listed in Table A.1. Values of those twelve parameters are used in this study across the oxidized PPy systems. Additionally, the CGFF electrostatic interactions follow the Wolf et al. [35] formulation in Eqs. (A.1) through (A.4), which besides the CG particle charges q and Q require two parameters pertaining to the simulation setup, κ and R_{cut}. The κ is a dumping term for suppressing the long range behavior of the Coulomb interactions. The R_{cut} represents the maximum distance up to which any interaction differs from zero and serves for evaluating $U_{cut} = \mathrm{erfc}(\kappa R_{cut})/R_{cut}$ in the aforementioned equations.

The protocol for determining the particle charges q, Q and values of the U_{inter} six parameters ϵ_{py-py}, σ_{py-py}, ϵ_{py-dop}, σ_{py-dop}, $\epsilon_{dop-dop}$, $\sigma_{dop-dop}$ in Eqs. (A.2), (A.3), (A.4) is based on density functional theory (DFT) at the B3PW91/6-311G(d) level. The Gaussian 16 [36] package is used for all DFT calculations in this study. The DFT electronic energy of provided PPy structures with dopants in conjunction with the electrostatic potential population analysis [37,38] is used for determining the charge transfer that occurs from the 12-Py oligomers to the halogen dopants. Determination of the best values for the U$_{inter}$ six parameters involves defining hundreds of DFT electronic energy target values of the oxidized PPy systems. The system structures used for generation of these DFT-based target values are gathered into a library [34], which is accessed for calculation of the classical potential energy through the CGFF model. Such setup enables for the non-linear least squares parameter optimization using the Levenberg–Marquardt algorithm [39].

2.2. The Metropolis Monte Carlo methodology

The Metropolis Monte Carlo (MMC) method [40] is an important sampling methodology extensively employed for the calculation of structural and thermodynamic properties of atomic and molecular systems. It is based on irreducible Markov chains for the stochastic evolution of the system particles ensuring the principle of detailed balance [41]. Hence, both the sampled space and the steps for changing the particle positions are discrete. The probability of obtaining a system configuration in equilibrium is given by the Boltzmann distribution, which is the limiting probability distribution to be sampled in the MMC. From the perspective of computational implementations, Markov chains are serial sequences not amenable to easy parallelization. Previous simulations in our group [34] dealt with a relatively small PPy system for which the isothermal–isobaric ensemble (NPT) MMC parallelization was implemented through a variant of the energy (farm) decomposition method [42]. Such approach is here generalized to evaluating the pair interactions by groups consistent with the various CGFF terms included in U$_{inter}$ and assigning their process to multiple GPUs.

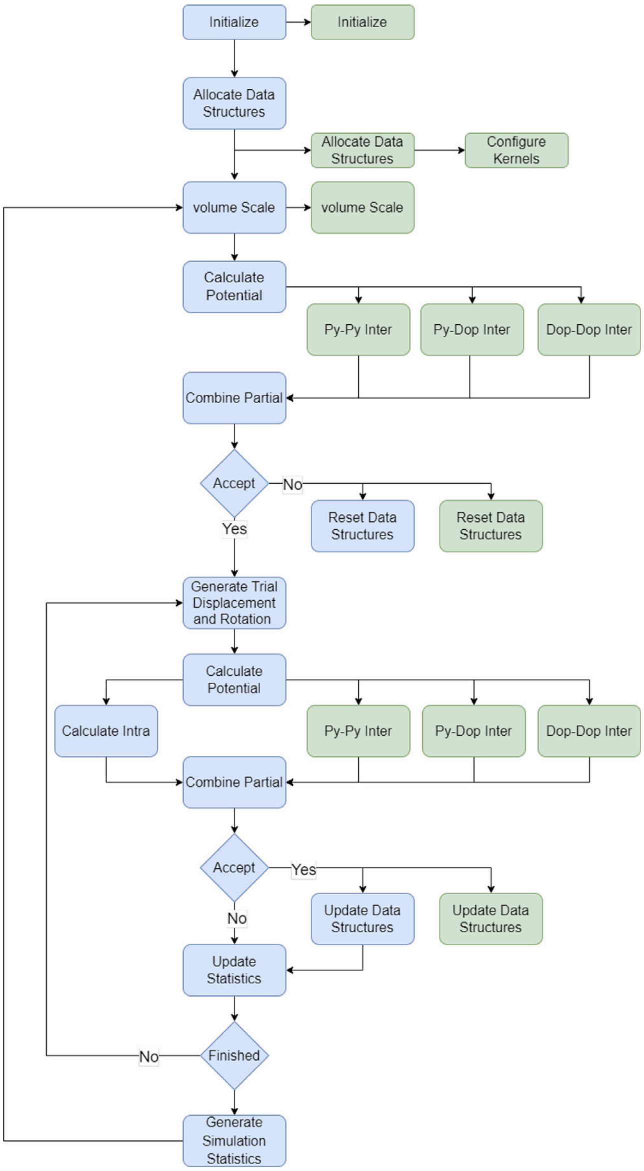

Fig. 2. Flowchart for the NPT-MMC implementation along one attempt of changing the system volume that triggers iterating over the particles in the system. Blue boxes represent work that is performed on the CPU and green boxes represent work that is performed on the GPUs.

A flowchart of the custom NPT-MMC simulation employed throughout is illustrated in Fig. 2 identifying the energy decomposition strategy along one MC iteration over the volume change which is followed by a sweep over all the system monomers and dopants. The implementation was initially developed in a workstation with four GPUs. Hence, the energy decomposition splits U$_{inter}$ into three terms, U$_{py-py}$ (Eq. (A.2)), U$_{py-dop}$ (Eq. (A.3)), U$_{dop-dop}$ (Eq. (A.4)) corresponding to oligomer–oligomer, oligomer–dopants, and dopant–dopant pairwise interactions, respectively. Meanwhile the U$_{intra}$ (Eq. (A.1)) and U$_{dipolar}$ (Eq. (A.5)) are calculated in the CPU. The scheme is easily extendable to computer platforms with multiple GPUs. The overall simulation workflow begins by reading an input file containing cyber and PPy system hyperparameters, CGFF parameter values, particles coordinates, and databases for the generation of the numeric approximation to the U$_{inter}$ analytical expression described in Section 3.2. Next the required data structures are initialized on the CPU. Along the initialization phase, particles in the system are decomposed into as many work-units as GPUs are detected in the hardware. Each GPU is assigned one work-unit containing all the information that a GPU will require for its initialization and processing. Once the initialization steps have completed, the simulation starts the MC loop. The first step of the simulation loop is to select a particle (monomer or dopant) and generate trial displacements and rotations for monomers or only trial displacements for dopants. Trial translational displacements of monomers and dopants are generated by providing the magnitude of the displacement vector and randomly assigning its orientation in spherical coordinates centered at each particle's center. For monomers, the possible rotation movements are generated randomly from the Euler angles [33,34]. To be successful, each monomer trial move needs to accept a rotation first in order to test for a translation displacement. Hence, both rotation and translation tested changes have to be successful for the move of monomers to take place. The generation of the trial particle motion is performed on the CPU and subsequently passed as parameters for calculation of the three above mentioned energy functions in U$_{inter}$, which are performed in parallel in the GPUs. Both U$_{intra}$ and U$_{dipolar}$ are calculated on the CPU/host in parallel with the GPUs calculation of the U$_{inter}$ terms. Overhead incurred from the CPU/host is masked by the time required by calculations in the GPUs. Since GPU kernels launches are asynchronous the U_{inter} calculations are launched first, while the CPU/host enters an OpenMP parallel section that involves energy functions associated to the oligomers alone. The next workflow step is collecting the various partial energy calculations in CPU–GPUs and perform the MC accept/reject criteria on the particle motion. If the trial particle move is accepted, then the data structures on the CPU/host and the GPU are updated. For each individual simulation, updating the data structures is performed last for performance reasons, since the protocol imposes a bias that maintains an acceptance rate fluctuating between 40% and 60% by having the ability of automatically and periodically modify the size of the particle moves (displacement/rotation) to control that the acceptance rate remains within its boundaries. Next, simulation statistics are updated for a sweep over all particles (included volume changes) followed by checking if the simulation has completed. If the simulation is not complete the process is repeated. Provided that a sufficiently large number of MC passages over the full system is performed along each simulation, the imposed bias of our implementation

Table 1
Developed parameter values for the electrostatic interactions in the CGFF of oxidized PPy with F, Br, I dopants that have a 3:1 monomer:dopant mixing concentration. U_{self} is a reference energy from the electrostatic interactions [35] to be added to total potential energies.

	F	Br	I
$Q_{transfer}$ (e)	3.5	3.3	3.2
q (e)	0.2917	0.275	0.2667
Q (e)	−0.875	−0.825	−0.8
κ (Å^{-1})	0.0983	0.0983	0.0983
R_{cut} (Å)	19.0	19.0	19.0
U_{self}/particle (eV)	−0.2046	−0.1819	−0.1710

Table 2
Values of the CGFF parameters in the term U_{inter}, Eqs. (A.2) through (A.4), determined along the optimization process. for oxidized PPy with Fl, Br, I dopants.

Parameter	F	Br	I
ϵ_{py-py} (eV)	0.136	0.136	0.136
σ_{py-py} (Å)	5.5	5.5	5.5
ϵ_{py-dop} (meV)	7.35	8.16	8.16
σ_{py-dop} (Å)	3.016	3.583	3.900
$\epsilon_{dop-dop}$ (eV)	2.721	2.721	2.721
$\sigma_{dop-dop}$ (Å)	4.868	4.868	4.868

avoids eventual trapping in metastable states. The NVT-MMC workflow is similar with the exception that the volume changes are eliminated and the probability of acceptance/rejection reverts to the elimination of the PV term in the probability distribution [41]. The custom code is available [43].

3. Results

3.1. Parametrization of the CGFF for oxidized PPy with halogen dopants

The CGFF mathematical expression provided in Appendix A describes the analytical representation of the interactions in U_{intra} and U_{inter}. Determination of the parameter values in these equations requires two stages. The first stage is based on the previously described DFT protocol [34] for determining values of parameters pertaining to the electrostatic interactions, namely, the monomer charge q, the dopant charge Q, and the dipole moment $\vec{\mu}$ in Eqs. (A.1) through (A.5). Imperative for determining q and Q is the calculation of $Q_{transfer}$, the charge transferred from the 12-Py oligomer to the dopants in systems with relative concentration monomer:dopant of 3:1. As a result, the monomer charge is $q = Q_{transfer}/12$ and the dopant charge is $Q = -Q_{transfer}/4$, as reported in Table 1. Throughout this study, every electrostatic interaction follows the Wolf et al. [35] formulation, which additionally requires the parameters κ and R_{cut} pertaining to the simulation setup. The κ is a dumping term for suppressing the long range behavior of the Coulomb interactions and R_{cut} is set in the simulation representing the maximum distance up to which any interaction differs from zero; the electrostatic interaction evaluated at R_{cut} is termed U_{cut} in Eqs. (A.1) through (A.4). In addition, the electrostatic interaction in [35] contains the self term U_{self} corresponding to the interaction of charges with themselves. The latter is a constant once the number of particles and their charges are set for each system under evaluation. In what follows, U_{self} has served as a reference value for energies, while energies/particle refer to the sum of all monomers plus all dopants in each system. The calculated values for this set of parameters and their derived constants for all oxidized PPy systems considered are listed in Table 1. k

In the second stage of the parameter optimization, the U_{inter} component of the CGFF has a crucial weight. Indeed, U_{inter} has four terms: U_{py-py} being the interaction between monomers in different oligomers, U_{py-dop} representing the interaction between oligomers and dopants, $U_{dop-dop}$ containing the dopant-to-dopant interactions, and $U_{dipolar}$ characterizing the dipole–dipole interaction between monomers in different oligomers. Their analytical expressions are given in Eqs. (A.2), (A.3), (A.4), (A.5), respectively, and contain six parameters to yet be determined: ϵ_{py-py}, σ_{py-py}, ϵ_{py-dop}, σ_{py-dop}, ϵ_{py-py}, σ_{py-py}. Values for these six parameters are obtained from a combined non-linear mean square fit to match ninety DFT binding energies of small PPy structures [34] followed by a reinforcement learning enhancement utilizing NPT-MMC simulations of the oxidized PPy system with 1024 particles at 300 K and 1 atm. The dual process, parameters from the fit plus simulation using them, is iterated until the RMSE reaches a stable low value and the system density resulting from the MMC simulation is consistent with empirical values. Such approach involves repetitive parameter values optimization (initialized differently) against the DFT target energies followed by the acceptance or rejection of such optimized parameter values set based on the MMC determination of the equilibrated system density. Additionally, for PPy oxidized by Cl dopants, the U_{py-dop} of Eq. (A.3) has an analytical modification to the previously reported mathematical expression [34] entailing new parameters ϵ_{py-dop}, σ_{py-dop} plus new κ's value. The final set of the six parameter values are reported in Table 2. Summarizing, an optimization RMSE of 5% was obtained when the target structures potential energies were calculated via the CGFF with values of its twenty two parameters listed in Tables 1, 2, and A.1.

The protocol developed in this study for defining the best parametrization of the analytical CGFF is predicted to be crucial for attaining future generalizations. There is confidence that the CGFF with its parameter value set enables a novel description of the oxidized PPy system that is prone to generalization for other similar polymers and/or other atomic or small molecular dopants. The characteristics of the CGFF are thus more general than the current representation of the oxidized PPy system.

3.2. Performance of the MMC simulations

Our customized parallelizing approach and CPU–GPU implementation of the MMC simulation yielded a performance gain factor between 3 and 15 on the processing time required for a single MMC trial (passage over all the oxidized PPy system particles) for systems containing less than 30 000 particles [42]. These performance metrics are for a single MMC trial whereas in the production stage of a regular simulation several millions of trials are required. As the system is scaled up in size it becomes evident that the overall execution time needs to be reduced by other means than parallelization. To reduce computational complexity and tackle the system size scalability, an approximation approach is developed for evaluating the three pairwise additive interactions U_{py-py}, U_{py-dop}, $U_{dop-dop}$ entering in U_{inter} (Eqs. (A.2), (A.3), (A.4)). The computational task can be simplified by creating a numerical table for each term with its pre-calculated values at predefined intervals of the distance between particles. In addition, piecewise interpolation polynomials are preassigned for automatically obtaining the term values at distances within the pre-defined intervals.

Several types of polynomials were considered for the polynomial interpolation approximation of Eqs. (A.2), (A.3), (A.4), including cubic splines, 3rd, and 6th order physicist's Hermite polynomials [44]. For performing the piecewise interpolation, the desired domain is discretized at chosen intervals of 5.29177×10^{-4} Å. These intervals may be adjusted in value to be either larger or smaller for increasing or decreasing the size of the database containing the polynomial coefficients. Once the domain has been discretized, starting at the first data point, four consecutive data points are taken, the coefficients of the interpolant are determined and stored in a database. This process is repeated for each interval of the discretized domain populating the database tables of interpolation coefficients for the successive discretized intervals. Separate databases of interpolation coefficients are generated for each of the three pairwise additive terms U_{py-py}, U_{py-dop}, $U_{dop-dop}$ of the CGFF. The database key is its first column of the

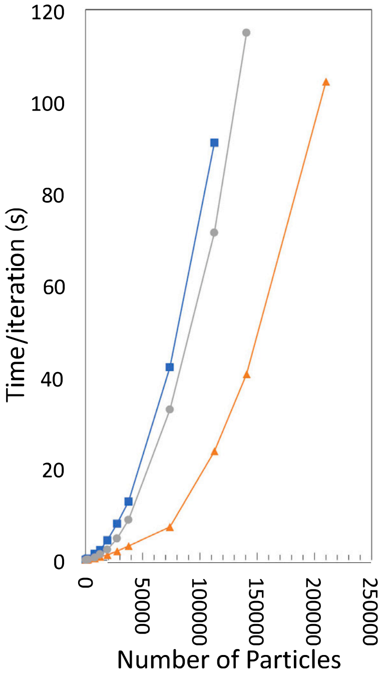

Fig. 3. Comparison of the MMC execution time of one passage over all particles for various oxidized PPy system sizes. *Red line* depicts the U_{inter} approximated by the polynomial interpolation executed in the GPU, while *gray line* depicts the execution in the CPU. The *blue line* illustrates the U_{inter} direct solver executed in the GPU.

discretized distance between particles. When entering the database of the desired function with a calculated distance between particles, its key directs to the interval that contains the entering distance value and leads to the table of interpolant coefficients appropriate for the approximated function. The interpolant is calculated and its value at the incoming distance is returned. The overall functional error that the polynomial approximations produced on the three terms of the CGFF is given in the SI, Table SI.2 and Fig. SI.1. Each generated database is loaded at simulation run-time to the CPU memory and to the assigned GPU memory, providing fast lookup times for the interpolation coefficients. Hence, along the simulation execution, when U_{inter} is calculated for the oxidized PPy system, instead of directly computing the analytical pairwise additive equations pertaining to U_{inter}, a simpler set of computations is performed by reading the tables in the three developed databases containing the appropriate interpolant coefficients. The $U_{dipolar}$ term, Eq. (A.5), is computed in the GPU from its mathematical expression.

In a nutshell, by simplifying the computational effort through the piecewise polynomial approximation a substantial improvement in execution time is achieved when compared to the full evaluation of the CGFF analytical expressions. Fig. 3 illustrates the execution time of one MMC passage over all the particles in systems with increasing number of particles. Although the number of operations in each case is of $O(N^3)$, it is clear from Fig. 3 that interpolation tables executed in the GPU (red line) are more efficient than either the GPU implementation of the direct solver methodology (blue line) or the CPU implementation of the approximation (gray line).

In yet another performance enhancement, either the CPU host or the GPU kernel that evaluate the CGFF functions calculate an array of trial particle movements for all the system particles at the beginning of any MMC passage over all particles. Nonetheless, the sequential selection of one particle at a time for the acceptance/rejection of their movement continues to be enforced. This approach reduces memory addressing and permits a high degree of memory reuse for distances values. Putting together these cyber enhancements, several MMC simulated properties of the polymer samples were analyzed for performance. For example, for an oxidized PPy system with 27 648 particles at 300 k and 1 atm, the density, enthalpy, and potential energy simulation values obtained after two million MMC passages over all the monomers and dopants are listed in Table SI.3. This comparison indicates the CGFF as calculated by the polynomial approximations yields simulated property values within the standard deviation from the direct solver for the calculated property values.

3.3. Size scaling stability of the oxidized PPy system

In molecular simulations an evaluation of the stability of properties as a function of scaling up the system size is relevant. Hence, several properties of the oxidized PPy by Cl dopants is tested for system sizes scaled up to 128 000 particles. Table 3 lists relevant properties at 300 K and 1 atm calculated from NPT-simulations consisting of 5×10^5 MMC passages over all particles to reach equilibrium and 10^6 additional passages for the calculation of averages and standard deviations. These simulations verify that crucial properties of the Cl oxidized PPy system rapidly converge to stable values as system size is scaled up.

The selected system sizes are based on a protocol of first equilibrating the small system with 1024 particles which is an orthorhombic, almost cubic box, and translate it n_{cell} = 1,2,3,4 times in each direction giving rise to the reported supercell sizes containing the number of particles listed in Table 3. These supercells were used as initial configurations for the NPT-MMC simulations giving rise to properties listed in Table 3. Results in this table demonstrate that the new MMC implementation scales very well to larger system sizes and generates consistent results across the scaled up system sizes. In addition, the piecewise polynomial interpolation for calculation of part of the CGFF does not cause a degradation in the properties values as can be seen in Table SI.3. The 12-Py oligomer structural properties are defined as previously published [34]. The values of radius of gyration, end-to-end distance, and Z order parameter demonstrate how rigid these polymer chains are. Values close to one of the vector order parameter S are clear evidence that there is a strong chain stacking order in the systems at the nanoscale.

3.4. Properties of the oxidized PPy system with halogen dopants

Considering that systems with either a mid-sized system with 8192 particles (6144 monomers and 2048 dopants) and/or a large size system with 27 648 particles (20 736 monomers with 6912 dopants) already display an excellent size stability of the involved MMC simulations, the thermodynamic and structural properties of the oxidized PPy with F, Br, and I dopants are calculated for the small, mid, and large size systems with the new CGFF parametrization from Tables 1 and 2.

Enthalpy, H, and density are thermodynamic properties that control the thermal stability of condensed systems. The H dependence with temperature is termed the caloric curve and serves for determining characteristic transition temperatures. Fig. 4 depicts H calculated at a set of temperatures of the oxidized PPy with the three halogen dopants obtained from the NPT-MMC simulations of the small, mid, and large size systems. Meanwhile, Fig. 4 (bottom) illustrates the temperature trend of the system densities at the same temperatures, system sizes, and for the three different dopants under study than those provided for enthalpy in Fig. 4 (top). Worth noting is that independently of the system size, the NPT-MMC simulations were always initiated from system models at densities significantly lower than the equilibrated densities at 300 K and 1 atm. As mentioned earlier, the system size scaling demonstrates the consistency of enthalpy and density for the PPy systems across the range 300 K–600 K. Meanwhile, Table 4 summarizes results at 300 K and 1 atm revealing as well the stability of potential energy values due to the system size increase. Indeed, Table 4 enumerates enthalpy, density and volume averages and their fluctuations. As expected, fluctuations decrease as the system size increases.

Table 3
Properties of Cl oxidized PPy systems with different sizes, from NPT-MMC simulations at 300 K and 1 atm. The 3rd order physicist's Hermite polynomial was used for the numerical approximation of U_{inter} with parameter values from Table A.1 The ± identifies one time the standard deviation.

Property | Number of Particles	8192	27 648	65 536	128 000
Enthalpy/particle (eV)	−3.3723 ± 0.0003	−3.3749 ± 0.0002	−3.3728 ± 0.0002	−3.3711 ± 0.0001
Density (kg/m^3)	1383.8 ± 0.7	1384.5 ± 0.5	1383.7 ± 0.3	1382.7 ± 0.2
Volume (nm^3)	568.1 ± 0.3	1916.4 ± 0.7	4545.2 ± 0.9	8883.5 ± 0.8
U_{total}/particle (eV)	−3.4111 ± 0.0003	−3.4138 ± 0.0002	−3.4117 ± 0.0002	−3.4099 ± 0.0001
U_{inter}/particle (eV)	−1.7055 ± 0.0003	−1.7084 ± 0.0002	−1.7062 ± 0.0002	−1.7043 ± 0.0001
U_{intra}/particle (eV)	−1.7056 ± 0.0003	−1.7054 ± 0.0002	−1.7054 ± 0.0001	−1.7056 ± 0.0001
Vector Order Parameter (S)	0.9999 ± 0.0000	0.9999 ± 0.0000	0.9999 ± 0.0000	0.9999 ± 0.0000
12-Py Orientation Order Parameter (Z)	0.7870 ± 0.0005	0.7870 ± 0.0006	0.7873 ± 0.0005	0.7872 ± 0.0005
12-Py Radius of Gyration (nm)	1.0911 ± 0.0002	1.0925 ± 0.0001	1.0925 ± 0.0001	1.0926 ± 0.0001
12-Py end-to-end distance (nm)	3.9535 ± 0.0007	3.9529 ± 0.0007	3.9523 ± 0.0003	3.9534 ± 0.0003

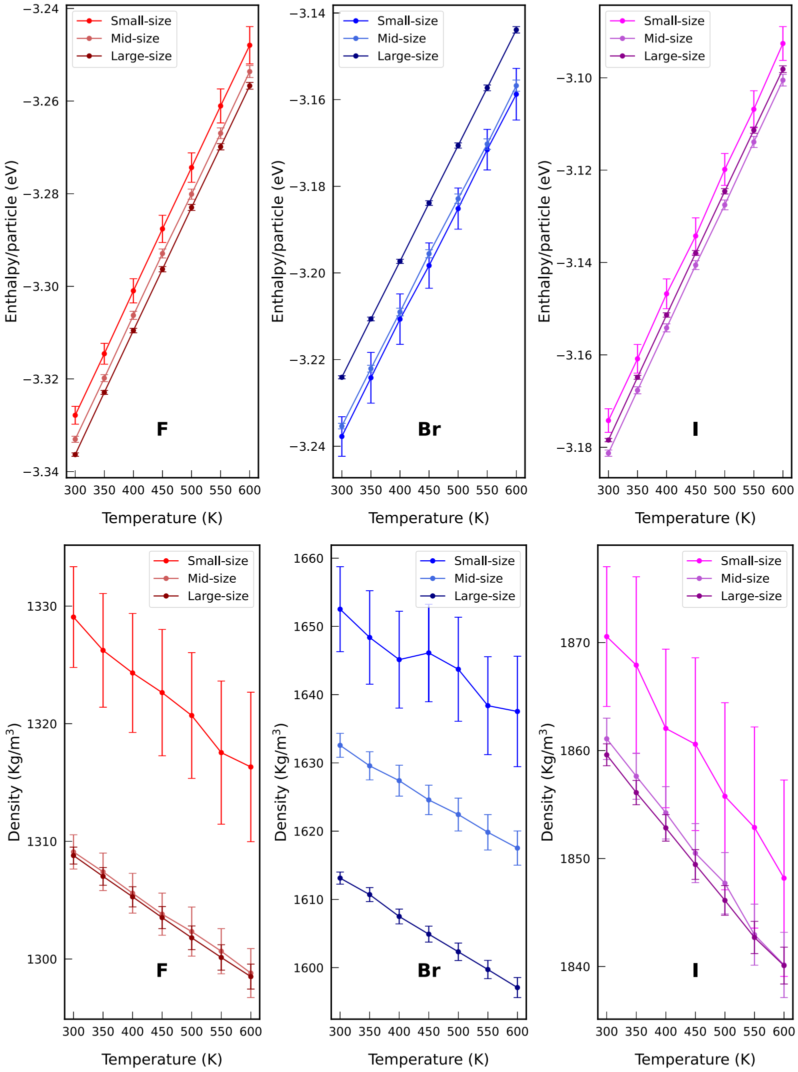

Fig. 4. Enthalpy per particle (top) and density (bottom) of the oxidized PPy small, mid, and large size systems with F (left), Br (center), I (right) dopants at different temperatures and 1 atm. Averages were calculated from the last 10^6 MMC passages through all system particles. Error bars depict twice the standard deviation. Color scheme: light colors identify the small system, intermediate shade colors depict the mid size system, dark colors pertain to the large system.

Within the NPT simulation approach, systems with demonstrated enthalpy (H) and the volume (V) stability enable calculation of properties from response functions such as the heat capacity at constant pressure $C_P = \left(\frac{\partial H}{\partial T}\right)_P$, the coefficient of thermal expansion CTE $= \frac{1}{V}\left(\frac{\partial V}{\partial T}\right)_P$, the compressibility $\beta_C = -\frac{1}{V}\left(\frac{\partial V}{\partial P}\right)_T$, and the bulk modulus $B=\beta_C^{-1}$. The glass transition temperature T_g is investigated as well. The PPy systems are rigid giving rise to small changes in the enthalpy and volume for small temperature or pressure variations. Hence, the response properties values are highly influenced by the fluctuations of H and/or V, which are responsible for their estimates with large fluctuations. Table 5 provides the calculated estimates of these response properties for the large size oxidized PPy systems. Due to the CGFF construction, the C_P estimates do not contain vibrational contributions of the eight actual atoms within each Py monomer. Consequently, calculated values of C_P are lower than empirical measurements [45,46], showing a decrease in value as the dopant mass increases. Estimates listed in Table 5 show a consistent slight increase in the CTE, β_C, and

Table 4

Thermodynamic and energy properties of the oxidized PPy small, mid, and large size systems with F, Br, I dopants at 300 K and 1 atm. The ± identifies one time the standard deviation.

	Small size	Mid size	Large size
Fluorine dopants			
Enthalpy/particle (eV)	−3.3278 ± 0.0009	−3.333 ± 0.0003	−3.3363 ± 0.0002
Density (kg/m^3)	1329 ± 2	1309.1 ± 0.7	1308.9 ± 0.3
Volume (nm^3)	68.6 ± 0.1	557.4 ± 0.3	1881.7 ± 0.5
U_{total}/particle (eV)	−3.3666 ± 0.0009	−3.3719 ± 0.0003	−3.3752 ± 0.0002
U_{inter}/particle (eV)	−1.6523 ± 0.0007	−1.6631 ± 0.0003	−1.6657 ± 0.0001
U_{intra}/particle (eV)	−1.7144 ± 0.0008	−1.7087 ± 0.0003	−1.7094 ± 0.0002
Bromine dopants			
Enthalpy/particle (eV)	−3.238 ± 0.003	−3.2354 ± 0.0003	−3.2241 ± 0.0002
Density (kg/m^3)	1652 ± 3	1633 ± 1	1613 ± 1
Volume (nm^3)	70.9 ± 0.1	573.9 ± 0.3	1960.1 ± 0.5
U_{total}/particle (eV)	−3.2765 ± 0.0028	−3.2742 ± 0.0003	−3.2629 ± 0.0002
U_{inter}/particle (eV)	−1.5592 ± 0.0028	−1.5611 ± 0.0003	−1.5536 ± 0.0001
U_{intra}/particle (eV)	−1.7173 ± 0.0009	−1.7131 ± 0.0003	−1.7094 ± 0.0002
Iodine dopants			
Enthalpy/particle (eV)	−3.174 ± 0.001	−3.1813 ± 0.0003	−3.1785 ± 0.0002
Density (kg/m^3)	1871 ± 3	1861 ± 1	1860 ± 0.5
Volume (nm^3)	73.3 ± 0.1	589.3 ± 0.3	1990.4 ± 0.5
U_{total}/particle (eV)	−3.213 ± 0.001	−3.2201 ± 0.0003	−3.2173 ± 0.0002
U_{inter}/particle (eV)	−1.500 ± 0.001	−1.5064 ± 0.0003	−1.5019 ± 0.0002
U_{intra}/particle (eV)	−1.7134 ± 0.0009	−1.7137 ± 0.0003	−1.7154 ± 0.0002

Table 5

Estimated properties of the oxidized PPy large size systems. Response properties CTE, β_C, B are from MMC simulations at 300 K and 1 atm. The C_P and the T_g temperature range are from the MMC simulated cooling along the 1 atm isobar, Figs. 5, 6.

Property	F dopants	Br dopants	I dopants
C_P below T_g (J/kg/K)	433 ± 21	337 ± 13	295 ± 13
C_P, above T_g (J/kg/K)	488 ± 21	372 ± 13	338 ± 13
CTE ($10^{-5} K^{-1}$)	2.7 ± 1.0	3.0 ± 1.1	3.9 ± 1.1
β_C (GPa^{-1})	1.46 ± 0.05	1.36 ± 0.16	1.23 ± 0.01
B (MPa)	686 ± 23	737 ± 78	811 ± 4
T_g range (K)	300–400	330–430	330–420

B as the mass of the dopant increases. Experimentally, as a function of increasing temperature the polymer samples undergo mass loss due to release of their constituent dopants or trapped water [45–49]. In fact, the empirically analyzed polymer samples are not infinitely extended as the models in our simulations. For example, empirical results of the CTE may be either positive [45,47] or negative [50] if the polymer sample contracts. Our CTE estimates in Table 5 are within the range of published positive values [45,47].

Oxidized PPy is synthesized either through chemical or electrochemical polymerization and is difficult to process after synthesis due to being a hard, non-thermoplastic material, brittle, not soluble in most common solvents, and non-degradable [51]. Moreover, the empirical reproducibility of the values for some properties depends on the preparation of the samples, on the dopant type, on the PPy samples aging and storage history, on the ambient humidity and water absorption of the polymer among other factors. For example, major applications require PPy thin films that display distinct surface properties if interfacing with the depositing material, with controlled gases, or with liquid environments. In most thermal experiments the loss of mass is substantial as temperature is increased with dopants able of evaporating from the samples [45,49]. For PPy, the glass transition temperatures T_g would occur within a range of temperatures when the polymer matrix is transitioning from a brittle solid to a softer rubbery state. However, due to the experimental constraints enumerated previously, the empirical determination of B and T_g has been elusive. Several published work has shown that for certain dopants their vaporization temperature coincides and masks the PPy process of transitioning from a brittle solid to a softer rubbery state [13,14,45,49]. In addition, as temperatures increase from ambient conditions, empirically the oxidized PPy samples decrease in mass losing dopants or adsorbed water and morphing into very inhomogeneous samples [13,14,45,49].

Conversely to the above mentioned empirical observations, from the perspective of our MMC simulations with constant number of particles, the oxidized PPy systems are infinite with no boundaries, thus, degradation by mass loss cannot occur. Nonetheless, the caloric curve H(T) of oxidized PPy with F, Br, I dopants was simulated by cooling these systems and bringing their temperature down from 600 K to 300 K along the 1 atm isobar as shown in Fig. 5. The simulated isobaric cooling process simultaneously provides V(T), the volume temperature profile, which enables calculation of the density temperature profile along the chosen isobar since the system mass is constant. Density versus temperature is displayed in Fig. 6 for the mid size systems and in Fig. SI.2 for the large size systems. From the simulation perspective, the isobaric cooling processes is a means for determining a temperature range where the glass transition temperature T_g occurs. Hence, T_g ranges were estimated by analyzing both density and enthalpy temperature trends along the isobaric cooling process. As shown in Figs. 5, 6 for enthalpy and density, the calculated points close to 300 K were fitted by a line and a second line was fitted on points closer to 600 K. The two fitted lines cross at a specific temperature and remain within the calculated points error bars up to two temperatures that enable a definition of the T_g temperature range reported in Table 5.

The C_P values below and above the T_g range included in Table 5 are calculated from the fitted lines to the enthalpy simulation points. As mentioned earlier, the enthalpy does not contain the vibrational energy contribution of the eight actual atoms inside each coarse grained monomer; consequently the enthalpy temperature profile is affected in both, the 300 K and 600 K simulated regions such that the C_P simulated values are not directly amenable to be compared with experiments. In contrast, the density thermal profiles shown in Fig. 6 and in Fig. SI.2 are a realistic outcome of these amorphous solids and would be comparable to empirical measurements implemented such that no loss of system mass occurs. We also note that the simulated isobaric cooling process in these oxidized PPy brittle systems yields smoother density and enthalpy thermal profiles as compared to those of more malleable polymers that display a larger change in the slope of the two fitted lines [52,53].

3.5. *The oxidized PPy structural properties*

The internal structure of the 12-Py oligomers maintained a remarkable similarity within the small, mid and large size systems as shown in Table SI.4. The oligomer radius of gyration, end-to-end distance, and Z order parameter are properties depending on the zig-zag planar conformation of the charged oligomer chain. These structural properties are negligibly affected by the difference in oligomer's charge for the oxidized PPy with F, Br, or I dopants investigated here. Indeed, although the dopants Q values follow the electronegativity pattern of halogen atoms as reported in Table 1, the simulations indicate that the highly charged 12-Py oligomers ($+3.2e$ through $+3.5e$) maintain the flat stick geometry across the system sizes investigated. The order parameter S = 1 from Table SI.4 evidences the oligomer chain stacking occurring for the three halogen dopants in the oxidized PPy systems, which persists as the system size increases. Despite the chain stacking, these oxidized PPy systems characterize as amorphous solids. For the large size system, Fig. 7 illustrates the radial distribution functions g(r) for the three particle pair types, monomer–monomer in different chains (red), monomer–dopant (green), and dopant–dopant (blue), depicting the functions up to distances of R_{cut} = 19 Å (Table 1). These functions display a well defined broad first shell of neighboring particles, significant smearing and broadening of subsequent peaks around function values of one signalizing both, the amorphous solid polymer structure and compliance with the asymptotic behavior of normalized functions. At distances larger than R_{cut}, particles do not interact, are maintained together by the collective effect of the condensed system with periodic boundary conditions that imposes a maximum distance attainable in the simulations of $V^{1/3}/2 \approx 62$ Å for the large systems at 300 K and volumes V from Table 4.

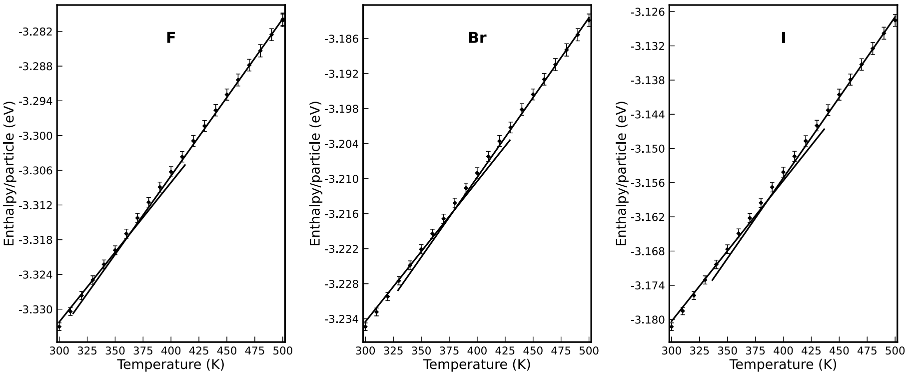

Fig. 5. Enthalpy of oxidized PPy with halogen dopants as a function of temperature along the 1 atm isobaric cooling process with a cooling rate of 9×10^{-6} K/(system passage) for the mid size systems. Averages and s.d. are from equilibrated simulations with 10^6 MMC passages over all particles in each system. The two straight lines are fits to the simulated values that cross at 362 K, 379 K, 388 K for systems with F, Br, I dopants, respectively.

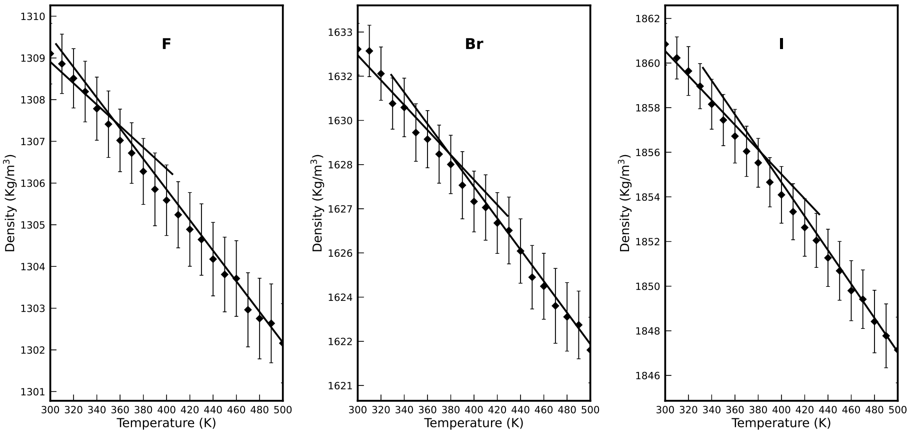

Fig. 6. Density of oxidized PPy with halogen dopants as a function of temperature along the 1 atm isobaric cooling process with a cooling rate of 9×10^{-6} K/(system passage) for the mid size systems. Averages and s.d. are from equilibrated simulations with 10^6 MMC passages over all particles in each system. Straight lines are fits to the simulated values that cross at 355 K, 379 K, 382 K for systems with F, Br, I dopants, respectively.

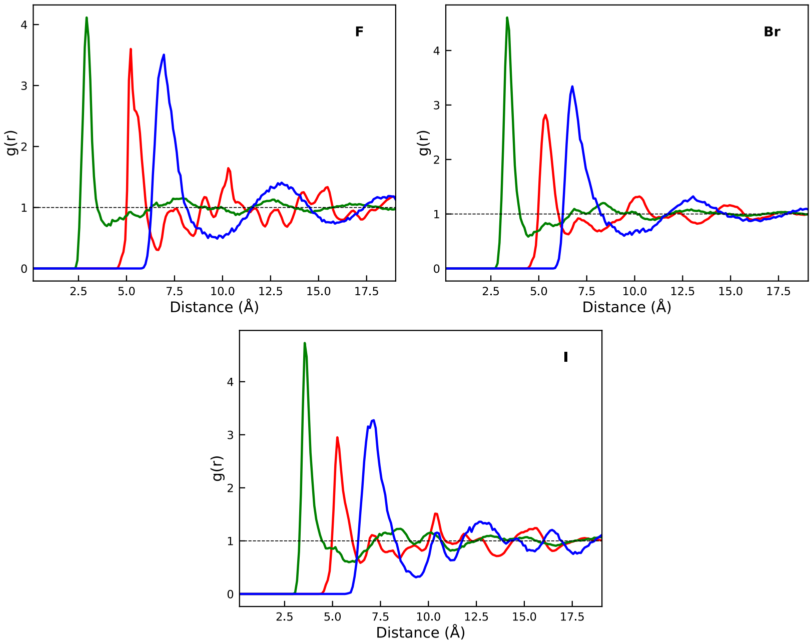

Fig. 7. Radial distribution functions g(r) of the oxidized PPy large size systems with halogen dopants at 300 K. Functions are calculated from NVT-MMC simulations at densities listed in Table 4 and depicted up to the R_{cut} distance from Table 1. Color scheme: red for monomer–monomer in different oligomers, green for monomer–dopant, blue for dopant–dopant.

4. Discussion

Modeling and simulation of polymer condensed phases is increasingly drawing the attention for applications where the polymer samples empirical reproducibility is challenging to be controlled. Evidence from multiple studies indicate that the synthesis and preparation of oxidized polypyrrole (PPy) leads to a diversity of employed samples such as pellets, thin films, nano particles among others, which need to be better characterized from a broader perspective.

Notably, the halogen dopants produce charge-transfer from the oligomers to the dopants by oxidizing the 12-Py oligomers with charges ranging from $+3.8e$, $+3.3e$, $+3.2e$ for the F, Br, I dopants, respectively, as obtained from the density functional approach B3LYP/6-111(d). The MMC simulations are therefore based on coarse grained particles, either PPy monomers or halogen dopants that are charged and remain charged along the simulation. This characteristic enhances a stacking of the oligomer chains and contributes to an increase of the samples density. We examined the case of a less-likely charge transfer with hypothetical dopants that would yield oligomer charges of $1e$ through $2.5e$. In these tested cases, the system density was lower, the stiffness of the oligomers was reduced, and the chain stacking became fuzzier as the transferred charge was lower. Based on these characterizations and on our previous density functional theory calculations [54], similar enthalpy per particle and density for longer oligomers such as 15-Py and 18-Py that maintain the 3:1 relative monomer:dopant concentration are foreseeable. On the other hand, in lab-synthesized samples mass loss occurs, either because of aging or because of temperature. Necessarily, any loss of mass would result in changes of the monomer:dopant relative concentration entailing inhomogeneities in the charge transfer process across the PPy samples. Sample's degradation is not included in our simulations, opening an avenue for further investigations.

The simulated isobaric cooling processes of the condensed samples from 600 K to 300 K displayed an almost linear decrease of the oxidized PPy system enthalpy as the temperature was decreased as shown in Fig. 5. In coordination with the density temperature profile along the simulated cooling of Fig. 6, we were able of predicting a temperature range of 300–400 K around T_g for the polymer samples to transition between the lower temperatures brittle structure to a more rubber-like structure at higher temperatures as reported in Table 5. Across the tested 300–600 K temperature span, the polymer samples are amorphous. Nonetheless, at the lower temperatures these systems display oligomer stacking within the sample volume evidenced by the vector order parameter S = 1, Table SI.4. The oligomer stacking has been observed in oxidized polypyrroles. The T_g temperature range is a prediction, since empirical T_g measurements have been elusive due to the oxidized PPy mass loss occurring within that temperature range.

Additionally, this work studied several relevant response functions that are commonly measured for other polymers but are scarce to find for oxidized PPy. At 300 K the CTE and the bulk modulus increase as the dopant mass increases while the compressibility decreases. The calculated fluctuations of these properties are large. Similarly as the dopants mass increase, the heat capacity C_P trend displays a slight increase, both below and above the T_g temperature range as shown in Table 5. Because of the coarse grained nature of the monomers, estimates of C_P as a function of temperature are not directly comparable to empirical observations from differential scanning calorimetry (DSC) up to temperatures where sample's mass loss is absent [45].

5. Conclusion

This study conducted a systematic analysis of bulk properties of oxidized PPy that are currently elusive in wet laboratories. Toward that goal, in this work we dramatically improved the custom computational implementation of MMC simulations that employed our previously developed CGFF parametrized for oxidized PPy with chlorine dopants [34]. Contemporarily, the CGFF was generalized by new parametrization of oxidized PPy systems with halogen dopants F, Br, and I. We demonstrate the substantial enhancement of the MMC simulations computational performance on two fronts: (i) addition of GPU–CPU approaches for the implementation of the MMC simulation, and (ii) building of databases enabling the analytical CGFF pair additive interaction terms to be approximated by the numerical representation of piecewise polynomial interpolation. Based on both advances, computational implementation and CGFF generalization, enabled the examination of multiple properties of condensed samples of the oxidized PPy with F, Br, I dopants in the range of 300 to 600 K at 1 atm as a function of the system size ranging from 1024 to 128 000 particles. The simulations demonstrate that the system size scaling rapidly reaches convergence around 8000 particles on the values of numerous thermodynamic and structural properties of the oxidized PPy samples independently of the dopant employed. The properties reported include enthalpy, density, T_g temperature range, coefficient of thermal expansion, bulk modulus, specific heat, structural properties including radial distribution function. These properties validate that oxidized PPy is a brittle, amorphous solid, displaying polymer chain stacking with an estimated temperature range for the glass transition T_g between 300–400 K.

Being the first generalization of the CGFF for oxidized PPy with different dopants, this study is a validation of the proposed force field model and its pursuing parametrization protocol. Further generalizations will require defining a dopant prototype to validate a feasible charge transfer mechanism consistent with the interacting PPy oligomers. We anticipate that, by combining the already developed CGFF protocol design, further generalization with additional dopant characteristics such as a molecular structure, the approach of this study provides an open avenue for considering unexplored pathways for the analyses of oxidized PPy in important applications.

CRediT authorship contribution statement

Greg Helmick: Writing - part of original draft, Validation, Software, Methodology, Investigation, Data curation. **Yoseph Abere:** Visualization, Validation, Methodology, Investigation, Formal analysis, Conceptualization. **Estela Blaisten-Barojas:** Writing - part or original draft, review & editing, Supervision, Resources, Project administration, Methodology, Investigation, Funding acquisition, Formal analysis, Conceptualization.

Declaration of competing interest

The authors declare that they have no known competing financial interests or personal relationships that could have appeared to influence the work reported in this paper.

Acknowledgments

All large-scale simulations were performed on the high performance computing clusters of the Office of Research Computing at George Mason University. Authors acknowledge the 100% dedicated use for this project of the 4-GPU high-level server facilitated by the Department of Computational and Data Sciences of George Mason University.

Appendix A. Analytical expression of the CGFF (Coarse Grained Force Field)

The CGFF represents the total potential energy U_{total} of the oxidized PPy system and is split into two major components, $U_{total} = U_{intra} + U_{inter}$ containing 22 parameters. The U_{intra} has twelve unique parameters developed previously [34], which are listed at the top in Table A.1. Five parameters developed in this work for PPy with Fl, B, and I dopants (Table 1, Section 3.1) and previously developed for Cl dopants (Table A.1) enter in both, U_{intra} and U_{inter}. These parameters are specific to the electrostatic interactions [35], which require the monomer (q) and dopant (Q) charges, the simulation cutoff radius R_{cut}, the κ damping constant, and the value of $U_{cut} = \mathrm{erfc}(\kappa R_{cut})/R_{cut}$. The U_{inter} has six unique parameters, which were developed in this work for the oxidized PPy with F, Br, and I dopants (Table 2, Section 3.1) and previously developed for Cl (Table A.1). The analytical expressions of U_{intra} and U_{inter} are given in Appendices A.1 and A.2, respectively.

A.1. The CGFF intra-oligomer interactions

The U_{intra} component of the CGFF is as follows:

$$\begin{aligned} U_{intra} = {} & D_e \sum_{i=1}^{11} \left[\left(1 - e^{-\alpha(\frac{r_{i,i+1}}{r_0} - 1)} \right)^2 - 1 \right] + k_\theta \sum_{i=1}^{10} \left(\cos(\theta_i) - \cos(\theta_0) \right)^2 \\ & + \sum_{i=1}^{9} \left[k_1 \left(1 - \cos\left(\gamma_{i,i+1} - \gamma_0 \right) \right) + k_2 \left(1 - \cos 2\left(\gamma_{i,i+1} - \gamma_0 \right) \right) \right] \\ & + \mathrm{k}_{lib} \sum_{i=2}^{11} \left[\left(\frac{\hat{e}_i \cdot \vec{r}_{i,i+1}}{\mathrm{r}_{i,i+1}} - \cos(\frac{\theta_0}{2}) \right)^2 + \left(\frac{\hat{e}_i \cdot \vec{r}_{i,i-1}}{\mathrm{r}_{i,i-1}} - \cos(\frac{\theta_0}{2}) \right)^2 \right] \\ & + \frac{q^2}{4\pi\epsilon_0} \sum_{i=1}^{8} \sum_{j=i+3}^{12} \left(\frac{\mathrm{erfc}(\kappa \mathrm{r}_{ij})}{\mathrm{r}_{ij}} - U_{cut} \right) \\ & + 2\epsilon_{exclude} \sum_{i=1}^{10} \sum_{j=i+2}^{12} \left[\left(\frac{\sigma_{exclude}}{\mathrm{r}_{ij}} \right)^9 - \frac{3}{2} \left(\frac{\sigma_{exclude}}{\mathrm{r}_{ij}} \right)^6 \right] \\ & + \frac{1}{4\pi\epsilon_0} \sum_{i=1}^{11} \sum_{j=i+1}^{12} \frac{1}{\mathrm{r}_{ij}^3} \left[\vec{\mu_\mathrm{i}} \cdot \vec{\mu_\mathrm{i}} - 3 \frac{(\vec{\mu_\mathrm{i}} \cdot \vec{\mathrm{r_{ij}}})(\vec{\mu_\mathrm{j}} \cdot \vec{\mathrm{r_{ij}}})}{\mathrm{r}_{ij}^2} \right] \end{aligned} \tag{A.1}$$

where $r_{i,i+1}$ are distances between two contiguous 12-Py monomers. Bending angles θ are enclosed by contiguous distances $r_{i,i+1}$ and $r_{i+1,i+2}$. Dihedral angles γ are formed by three contiguous distances. The fourth term is a hindered rotation of each oligomer monomer in its plane around the normal vector centered at its center of mass; the oligomer end monomers do not librate. The fifth term is the electrostatic interaction between two oligomer monomers that are third or farther away neighbors. The sixth term sets an excluded volume when each monomer interacts with the second nearest and farther away neighbors. The seventh term represents the dipole–dipole interaction between the monomers in the 12-Py oligomer. The parameter values entering in U_{intra} are listed in Table A.1 and Section 3.1, Table 1.

A.2. The CGFF inter-particle interactions

The CGFF inter-particle interaction has four terms: $U_{inter} = U_{py-py} + U_{py-dop} + U_{dop-dop} + U_{dipolar}$. The first three terms are pairwise additive, while the fourth term is three-body additive. The number of different particles is termed N_{py} for monomers and N_{dop} for dopants. The analytical expressions for the four terms of U_{inter} are as follows:

$$\begin{aligned} U_{py-py} = {} & \frac{q^2}{4\pi\epsilon_0} \sum_{i=1}^{N_{py}-1} \sum_{j=i+1}^{N_{py}} \left(\frac{\mathrm{erfc}(\kappa R_{ij})}{R_{ij}} - U_{cut} \right) \\ & + 2\epsilon_{py-py} \sum_{i=1}^{N_{py}-1} \sum_{j=i+1}^{N_{py}} \left[\left(\frac{\sigma_{py-py}}{R_{ij}} \right)^9 - \frac{3}{2} \left(\frac{\sigma_{py-py}}{R_{ij}} \right)^6 \right] \end{aligned} \tag{A.2}$$

$$\begin{aligned} U_{py-dop} = {} & \frac{qQ}{4\pi\epsilon_0} \sum_{i=1}^{N_{py}} \sum_{s=1}^{N_{dop}} \left(\frac{\mathrm{erfc}(\kappa \mathrm{R}_{is})}{R_{is}} - U_{cut} \right) \\ & + 2\epsilon_{py-dop} \sum_{i=1}^{N_{py}} \sum_{s=1}^{N_{dop}} \left[\left(\frac{\sigma_{py-dop}}{R_{is}} \right)^9 - \frac{3}{2} \left(\frac{\sigma_{py-dop}}{R_{is}} \right)^6 \right] \end{aligned} \tag{A.3}$$

$$U_{dop-dop} = \sum_{i=1}^{N_{dop}-1} \sum_{j=i+1}^{N_{dop}} \left[\epsilon_{dop-dop} \left(\frac{\sigma_{dop-dop}}{r_{ij}} \right)^9 + \frac{Q^2}{4\pi\epsilon_0} \left(\frac{\mathrm{erfc}(\kappa \mathrm{r}_{ij})}{r_{ij}} - U_{cut} \right) \right] \tag{A.4}$$

Table A.1
Parameter values of the CGFF in Eqs. (A.1)–(A.5). The 12 parameters listed first are common for oxidized PPy with F, Cl, Br, I dopants. The reminding parameters and functions were developed previously for oxidized PPy with Cl dopants [34].

D_e (eV)	2.6921
r_0 (Å)	3.78569
α (Å^{-1})	3.32146
k_θ (eV)	26.12
θ_0 (degree)	141.576
k_1 (eV)	0.0548
k_2 (eV)	0.3795
γ_0 (degree)	180
k_{lib} (eV)	21.35
μ (D)	1.4126
$\epsilon_{exclude}$ (eV)	0.0759
$\sigma_{exclude}$ (Å)	8.9574
$Q_{transfer}$ (e)	4.0
q (e)	0.333
Q (e)	−1.0
κ (Å^{-1})	0.1134
R_{cut} (Å)	19.0
U_{self}/particle (eV)	−0.3074
ϵ_{py-py} (eV)	0.136
σ_{py-py} (Å)	5.5
A for $py-dop$ (meV)	36.319
B for $py-dop$ (meV)	43.757
σ_{old} for $py-dop$ (Å)	3.614
$\epsilon_{dop-dop}$ (eV)	2.967
$\sigma_{dop-dop}$ (Å)	4.909

$$U_{dipolar} = \frac{1}{4\pi\epsilon_0} \sum_{i=1}^{N_{py}-1} \sum_{j=i+1}^{N_{py}} \frac{1}{R_{ij}^3} \left[\vec{\mu_i} \cdot \vec{\mu_i} - 3 \frac{(\vec{\mu_i} \cdot \vec{r_{ij}})(\vec{\mu_j} \cdot \vec{r_{ij}})}{R_{ij}^2} \right] \tag{A.5}$$

where R_{ij} are the distances between the monomers center of mass and either monomers in other oligomers or dopants, r_{ij} are distances between dopants, q and Q (Tables 1 and A.1) are the monomer and dopant charges, respectively. The magnitude of monomers' dipole moment μ is given in Table A.1. The second term in Eq. (A.3) is the current CGFF analytical replacement to our previous [34] dispersion term $[A(\sigma_{old}/R)^9 \text{ -} B(\sigma_{old}/R)^6]$ with parameters A, B, σ_{old} for PPy with Cl dopants (see Table A.1).

Appendix B. Supplementary information

Supplementary material related to this article can be found online at https://doi.org/10.1016/j.commatsci.2024.113538.

Data availability

Scripts, codes, databases, and simulation input files underlying this study are in the openly available [43].

References

[1] L. Alcácer, Electronic Structure of Organic Semiconductors, Polymers and Small Molecules, 2053-2571, Morgan & Claypool Publishers, 2018, http://dx.doi.org/10.1088/2053-2571/aaddd8.

[2] M.I. Inamuddin, B. Ahamed, A.A. Gobouri, Electroactive Polymeric Materials, CRC Press, 2022, http://dx.doi.org/10.1201/9781003173502.

[3] G. Mittal, V. Dhand, K.Y. Rhee, S.-J. Park, W. Lee, A review on carbon nanotubes and graphene as fillers in reinforced polymer nanocomposites, J. Ind. Eng. Chem. 21 (2015) 11–25, http://dx.doi.org/10.1016/j.jiec.2014.03.022.

[4] G. Kaur, R. Adhikari, P. Cass, M. Bown, T. Gunatillake, Electrically conductive polymers and composites for biomedical applications, RSC Adv. 5 (2015) 37553–37567, http://dx.doi.org/10.1039/C5RA01851J.

[5] W. Zheng, P.G. Whitten, G.M. Spinks, Polypyrrole actuators: the effects of polymer thickness and voltage scan rate on fractional charging and isotonic actuation strain, Multifunct. Mater. 1 (2018) 014002, http://dx.doi.org/10.1088/2399-7532/aae3e0.

[6] R. Kiebooms, R. Menon, K. Lee, Chapter 1 - synthesis, electrical, and optical properties of conjugated polymers, in: H. Singh Nalwa (Ed.), Handbook of Advanced Electronic and Photonic Materials and Devices, Academic Press, Burlington, 2001, pp. 1–102, http://dx.doi.org/10.1016/B978-012513745-4/50064-0.

[7] K. Namsheer, C.S. Rout, Conducting polymers: a comprehensive review on recent advances in synthesis, properties and applications, RSC Adv. 11 (2021) 5659, http://dx.doi.org/10.1039/d0ra07800.

[8] A. Yussuf, M. Al-Saleh, S. Al-Enezi, G. Abraham, Synthesis and characterization of conductive polypyrrole: The influence of the oxidants and monomer on the electrical, thermal, and morphological properties, Int. J. Polym. Sci. 2018 (1) (2018) 4191747, http://dx.doi.org/10.1155/2018/4191747.

[9] A. Imani, M. Ghadim, G. Farzi, Synthesis of PPy-silver nanocomposites via in situ oxidative polymerization, J. Nanostruct. Chem. 4 (2014) 101, http://dx.doi.org/10.1007/s40097-014-0101-6.

[10] J. Fonner, C. Schmidt, P. Ren, A combined molecular dynamics and experimental study of doped polypyrrole, Polymer 51 (21) (2010) 4985–4993, http://dx.doi.org/10.1016/j.polymer.2010.08.024.

[11] G. Ozin, Nanochemistry: synthesis in diminishing dimensions, Adv. Mater. 4 (1992) 612–649, http://dx.doi.org/10.1002/adma.19920041003.

[12] E. Smela, Conjugated polymer actuators conjugated polymer actuators for biomedical applications, Adv. Mater. 15 (2003) 481–494.

[13] E.T. Kang, T.C. Tan, K.G. Neoh, Y.K. Ong, Halogen-induced charge transfer polymerization of pyrrole in aqueous media, Polymer 27 (1986) 1958–1962, http://dx.doi.org/10.1016/0032-3861(86)90189-8.

[14] K.G. Neoh, T.C. Tan, E.T. Kang, Chemical synthesis and characterization of polypyrrole-chlorine complex, Polymer 29 (1988) 553–558, http://dx.doi.org/10.1016/0032-3861(88)90377-1.

[15] C.K. Arakawa, C.A. DeForest, Chapter 19 - polymer design and development, in: A. Vishwakarma, J.M. Karp (Eds.), Biology and Engineering of Stem Cell Niches, Academic Press, Boston, USA, 2017, pp. 295–314, http://dx.doi.org/10.1016/B978-0-12-802734-9.00019-6.

[16] Y. Dai, C. Wei, E. Blaisten-Barojas, Bipolarons and polaron pairs in oligopyrrole dications, Comput. Theor. Chem. 993 (2012) 7–12, http://dx.doi.org/10.1016/j.comptc.2012.05.018.

[17] G. Jeon, S. Yang, J. Byun, K. Kim, Electrically actuatable smart nanoporous membrane for pulsatile drug release, Nano Lett. 11 (2011) 1284–1288, http://dx.doi.org/10.1021/nl104329y.

[18] J. Pan, Scaling up system size in materials simulation, Nat. Comput. Sci. 1 (2) (2021) 95, http://dx.doi.org/10.1038/s43588-021-00034-x.

[19] C. Choudhury, P. Carbone, S. Roy, Scalability of coarse-grained potentials generated from iterative Boltzmann inversion for polymers: Case study on polycarbonates, Macromol. Theory Simul. 25 (2016) 274–286, http://dx.doi.org/10.1002/mats.201500079.

[20] W. Wang, R. Gómez-Bombarelli, Coarse-graining auto-encoders for molecular dynamics, NPJ Comput. Mater. 5 (2019) 125, http://dx.doi.org/10.1038/s41524-019-0261-5.

[21] J. Jin, S.J. Turner, B.-S. Lee, J. Zhong, B. He, HPC simulations of information propagation over social networks, Procedia Comput. Sci. 9 (2012) 292–301, http://dx.doi.org/10.1016/j.procs.2012.04.031.

[22] R. Wyrzykowski, B.K. Szymanski, Taming next-generation HPC systems: Run-time system and algorithmic advancements, Concurr. Comput. Pract. Exp. 33 (2021) e6153, http://dx.doi.org/10.1002/cpe.6153.

[23] Y. Nejahi, M. Soroush Barhaghi, J. Mick, B. Jackman, K. Rushaidat, Y. Li, L. Schwiebert, J. Potoff, GOMC: GPU optimized Monte Carlo for the simulation of phase equilibria and physical properties of complex fluids, SoftwareX 9 (2019) 20–27, http://dx.doi.org/10.1016/j.softx.2018.11.005.

[24] J. Mick, E. Hailat, V. Russo, K. Rushaidat, L. Schwiebert, J. Potoff, GPU-accelerated gibbs ensemble Monte Carlo simulations of Lennard–Jonesium, Comput. Phys. Commun. 184 (2013) 2662–2669, http://dx.doi.org/10.1016/j.cpc.2013.06.020.

[25] T.-S. Lee, D.S. Cerutti, D. Mermelstein, C. Lin, S. LeGrand, T.J. Giese, A. Roitberg, D.A. Case, R.C. Walker, D.M. York, GPU-accelerated molecular dynamics and free energy methods in Amber18: Performance enhancements and new features, J. Chem. Inform. Model. 58 (10) (2018) 2043–2050, http://dx.doi.org/10.1021/acs.jcim.8b00462.

[26] M. Abraham, T. Murtola, R. Schulz, S. Pall, J. Smith, B. Hess, E. Lindahl, GROMACS: High performance molecular simulations through multi-level parallelism from laptops to supercomputers, SoftwareX 1–2 (2015) 19–25, http://dx.doi.org/10.5281/zenodo.11148638.

[27] A.P. Thompson, H.M. Aktulga, R. Berger, D.S. Bolintineanu, W.M. Brown, P.S. Crozier, P.J. in 't Veld, A. Kohlmeyer, S.G. Moore, T.D. Nguyen, R. Shan, M.J. Stevens, J. Tranchida, C. Trott, S.J. Plimpton, LAMMPS - a flexible simulation tool for particle-based materials modeling at the atomic, meso, and continuum scales, Comput. Phys. Commun. 271 (2022) 108171, http://dx.doi.org/10.1016/j.cpc.2021.108171.

[28] A. Donaldson, G. Gopalakrishnan, N. Chong, J. Ketema, G. Li, P. Li, A. Lokhmotov, S. Qadeer, Chapter 1 - formal analysis techniques for reliable GPU programming: current solutions and call to action, in: H. Sarbazi-Azad (Ed.), Advances in GPU Research and Practice, Emerging Trends in Computer Science and Applied Computing, Morgan Kaufmann, Boston, USA, 2017, pp. 3–21, http://dx.doi.org/10.1016/B978-0-12-803738-6.00001-X.

[29] S. Borkar, A. Chien, The future of microprocessors, Commun. ACM 54 (2011) 67–77, http://dx.doi.org/10.1145/1941487.1941507.

[30] S. Wolf, B. Lickert, S. Bray, G. Stock, Multisecond ligand dissociation dynamics from atomistic simulations, Nature Commun. 11 (1) (2020) 2918, http://dx.doi.org/10.1038/s41467-020-16655-1.

[31] T.E. Gartner III, A. Jayaraman, Modeling and simulations of polymers: A roadmap, Macromolecules 52 (2019) 758–786, http://dx.doi.org/10.1021/acs.macromol.8b01836.

[32] Y. Dai, E. Blaisten-Barojas, Monte Carlo study of oligopyrroles in condensed phases, J. Chem. Phys. 133 (2010) 034905, http://dx.doi.org/10.1063/1.3457675.

[33] C. Hall, X. Ji, E. Blaisten-Barojas, The Metropolis Monte Carlo method with CUDA enabled graphic processing units, J. Comput. Phys. 258 (2014) 871–879, http://dx.doi.org/10.1016/j.jcp.2013.11.012.

[34] Y. Abere, G. Helmick, E. Blaisten-Barojas, Modeling oxidised polypyrrole in the condensed phase with a novel force field, J. Phys.: Condens. Matter. 34 (2022) 185701, http://dx.doi.org/10.1088/1361-648X/ac303b.

[35] D. Wolf, P. Keblinski, S. Phillpot, J. Eggebrecht, Exact method for the simulation of Coulombic systems by spherically truncated, pairwise r^{-1} summation, J. Chem. Phys. 110 (1999) 8254–8282, http://dx.doi.org/10.1063/1.478738.

[36] M.J. Frisch, G.W. Trucks, H.B. Schlegel, G.E. Scuseria, M.A. Robb, J.R. Cheeseman, et al., Gaussian 16, revision C.01, 2016, Gaussian, Inc., Wallingford CT, USA.

[37] U.C. Singh, P.A. Kollman, An approach to computing electrostatic charges for molecules, J. Comput. Chem. 5 (1984) 129–145, http://dx.doi.org/10.1002/jcc.540050204.

[38] B.H. Besler, K.M. Merz Jr., P.A. Kollman, Atomic charges derived from semiempirical methods, J. Comput. Chem. 11 (1990) 431–439, http://dx.doi.org/10.1002/jcc.5400110404.

[39] Visual Numerics, Inc., San Ramon, CA, USA, IMSL mathematical functions in fortran, 2004, https://help.imsl.com/fortran/6.0/math/default.htm?turl=bclsf.htm; (Accessed 31 May 2024).

[40] N. Metropolis, A.W. Rosenbluth, M.N. Rosenbluth, A.H. Teller, E. Teller, Equation of state calculations by fast computing machines, J. Chem. Phys. 21 (6) (1953) 1087–1092, http://dx.doi.org/10.1063/1.1699114.

[41] D. Frenkel, B. Smit, Understanding Molecular Simulation : from Algorithms to Applications, second ed., in: Computational Science Series; 1, Academic Press, San Diego, USA, 2002.

[42] G. Helmick, Y. Abere, E. Blaisten-Barojas, The caloric curve of polymers from the adaptive tempering Monte Carlo method, in: Advances in Parallel and Distributed Processing and Applications, Springer Nature, London, England, 2021, pp. 253–260, http://dx.doi.org/10.1007/978-3-030-69984-0_19.

[43] G. Helmick, Y. Abere, E. Blaisten-Barojas, Size scalability of Monte Carlo simulations applied to oxidized PPy systems: Open access code and scripts, 2024, http://dx.doi.org/10.5281/zenodo.13826278.

[44] T.H. Koornwinder, R.S.C. Wong, R. Koekoek, R.F. Swarttouw, Chapter 18: Orthogonal polynomials, in: D.M. Olver, R.F. Boisvert, C.W. Clark (Eds.), NIST Handbook of Mathematical Functions, Cambridge University Press, New York, USA, 2010, pp. 435–484.

[45] A. Rudajevová, M. Varga, J. Proke, J. Kopecká, J. Stejskald, Thermal properties of conducting polypyrrole nanotubes, Acta Phys. Pol. A 128 (4) (2015) 730–736, http://dx.doi.org/10.12693/APhysPolA.128.730.

[46] B. Lunn, J. Unsworth, N. Booth, P. Innis, Determination of the thermal conductivity of polypyrrole over the temperature range 280–335 K, J. Mater. Sci. 28 (September) (1993) 5092–5098, http://dx.doi.org/10.1007/BF00361185.

[47] O. Sul, S. Jang, E. Yang, Determination of mechanical properties and actuation behaviors of polypyrrole-copper bimorph nanoactuators, IEEE Trans. Nanotechnol. 10 (5) (2011) 985–990, http://dx.doi.org/10.1109/TNANO.2010.2090667.

[48] M.F. Ghadim, A. Imani, G. Farzi, Synthesis of PPy-silver nanocomposites via in situ oxidative polymerization, J. Nanostruct. Chem. 4 (2014) 101, http://dx.doi.org/10.1007/s40097-014-0101-6.

[49] B.C. Ennis, V.-T. Truong, Thermal and electrical stability of polypyrrole at elevated temperatures, Synth. Met. 59 (1993) 387–399, http://dx.doi.org/10.1016/0379-6779(93)91170-7.

[50] J. Lin, Effect of polypyrrole deposition of carbon fiber on the thermal expansion of carbon fiber-epoxy composites, J. Polym. Res. 6 (4) (1999) 237–242, http://dx.doi.org/10.1007/s10965-006-0093-0.

[51] S. Meng, M. Rouabhia, G. Shi, Z. Zhang, Heparin dopant increases the electrical stability, cell adhesion, and growth of conducting polypyrrole/poly(L,L-lactide) composites, J. Biomed. Mater. Res. Part A 87 (2008) 332–344, http://dx.doi.org/10.1002/jbm.a.31735.

[52] J.P. Andrews, R.A. Handler, E. Blaisten-Barojas, Structure, energetics and thermodynamics of PLGA condensed phases from molecular dynamics, Polymer 206 (2020) 122903, http://dx.doi.org/10.1016/j.polymer.2020.122903.

[53] D. Sponseller, E. Blaisten-Barojas, Solutions and condensed phases of PEG2000 from all-atom molecular dynamics, J. Phys. Chem. B 125 (2021) 12892–12901, http://dx.doi.org/10.1021/acs.jpcb.1c06397.

[54] Y. Dai, E. Blaisten-Barojas, Energetics, structure, and charge distribution of reduced and oxidized N-pyrrole oligomers: A density functional approach, J. Chem. Phys. 129 (2008) 164903, http://dx.doi.org/10.1063/1.2996297.